

True amplitude depth migration using curvelets

Hamideh Sanavi¹, Peyman P. Moghaddam¹, and Felix J. Herrmann²

ABSTRACT

We have developed a true amplitude solution to the seismic imaging problem. We derive a diagonal scaling approach for the normal operator approximation in the curvelet domain. This is based on the theorem that states that curvelets remain approximately invariant under the action of the normal operator. We use curvelets as essential tools for approximation and

inversion. We also exploit the theorem that states that the curvelet-domain approximation should be smooth in phase space by enforcing the smoothness of curvelet coefficients in the angle and space domains. We analyze our method using a reverse time migration-demigration code, simulating the acoustic wave equation on different synthetic models. Our method produces a good resolution with reflecting dips, reproduces the true amplitude reflectors, and compensates for incomplete illumination in seismic images.

INTRODUCTION

Modern depth migration methods can accurately position reflecting events in the earth's subsurface. However, these methods often do not correctly resolve the amplitudes, which is true even when accurate knowledge of the velocity model is available. This comes from the fact that the migration operator is the adjoint but not the inverse of the modeling operator, with the modeling operator acting as the operator that maps the subsurface reflectivities to the recorded seismic data (see, e.g., Tarantola, 1984; Claerbout, 1992; Gray, 1997; Chauris and Cocher, 2017). Researchers have proposed three main approaches to derive true-amplitude migration schemes.

The first approach is the in-the-migration approach for correcting amplitudes. In this scheme, corrections are made during migration by modifying the imaging condition that corrects the reflector amplitudes (see, e.g., Zhang et al., 2007; Chattopadhyay and McMechan, 2008; Schleicher et al., 2008; Costa et al., 2009; da Silva Neto et al., 2011; Yang et al., 2015). Some researchers propose to define an approximate inverse operator for reverse time migration (RTM) (Hou and Symes, 2015; Chauris and Cocher, 2017; Li and Chauris, 2018), with the asymptotic approximation of the inverse operator using a pure wave-equation-based expression.

Second, the fact that the migration operator is the adjoint but not the (pseudo-)inverse of the scattering operator (see, e.g., Claerbout, 1992; Gray, 1997; Guitton, 2004; Symes, 2007; Herrmann and Li., 2012) leads to a second category of methods. In these methods, a variety of algorithms for true-amplitude migration have been introduced, which iteratively (using Lanczos or other linear algebra methods) update the migrated image (see, e.g., Tarantola, 1984; Kuel and Sacchi, 2003; Mulder and Plessix, 2004; Lu et al., 2017).

Third, there are the so-called image-to-image scaling methods, in which a scaling method is proposed for approximation of the Hessian (normal operator). The scaling is done by comparing the migrated image (with some possible pre-/postprocessing) with a remigrated image (i.e., applying the normal operator on the migrated image).

Typically, scaling is performed in some transform domains. The aim is to choose the scaling domain that can capture most important properties of the normal operator, namely, scattering point location invariance, compact support in the Fourier domain, invariance under the curvelet transform, etc. (see, e.g., Rickett, 2003; Guitton, 2004; Plessix and Mulder, 2004; Herrmann et al., 2008; Symes, 2008). Likewise, Liu and Peter (2018) propose a method to define the matching filter in the data domain for image-to-image scaling

Manuscript received by the Editor 31 May 2019; revised manuscript received 26 February 2021; published ahead of production 17 April 2021; published online 12 July 2021.

¹Ferdowsi University of Mashhad, Faculty of Sciences, Razavi Khorasan 9177948974, Iran. E-mail: hamidehsanavi@gmail.com; ppm1407@hotmail.com (corresponding author).

²University of British Columbia, Seismic Laboratory for Imaging and Modeling, Department of Earth and Ocean Sciences, British Columbia V6T 1Z4, Canada and Georgia Institute of Technology, Earth and Atmospheric Sciences, Atlanta, Georgia 30332, USA. E-mail: felix.herrmann@gatech.edu.

© 2021 Society of Exploration Geophysicists. All rights reserved.

methods. Our method falls into this category of using curvelets as transform domain scaling.

Recently, there has been some attention toward curvelet-domain scaling methods by Wang et al. (2016, 2017). One of the major differences between this study and previous work in this area is using the result of the theorem that states that curvelets are almost invariant under the action of the normal operator (Herrmann et al., 2008). Therefore, curvelets can be considered as the eigenvector for the normal operator, and we can represent it in a quasieigenvalue and eigenvector form with curvelets as the eigenvectors (Herrmann et al., 2008).

Another difference between this approximation and the curvelet-domain approximation used by Wang et al. (2016, 2017) is that the match is performed from the reference image to the approximate image in the physical domain rather than in the curvelet domain. Matching in the physical domain is more preferable than that in the curvelet domain because the latter generally leaves some artifacts behind due to curvelet coefficient truncation. In general, a large curvelet coefficient will leave a curvelet-like artifact in the physical domain.

The main contributions of this paper compared to the earlier work of Herrmann et al. (2008) are threefold. First, we replace the linear least-squares formulation for estimation of the curvelet domain coefficients (Herrmann et al., 2008) by a nonlinear least-squares formulation, which imposes positivity on the scaling coefficients. This comes from the fact that the normal operator is positive semidefinite. Second, we impose smoothness constraints on the scaling curvelet coefficients in physical and phase spaces to exploit the theorem (Herrmann et al., 2008), which states that symbols of the normal operator (in this case, curvelet coefficients) are smooth. Third, we remove the necessity for a second optimization (namely, stable amplitude recovery with the L1 norm) because we estimate the inverse of the normal operator directly and do not need to invert it anymore.

We start with a short review explaining the theoretical underpinning of image-to-image scaling methods. Then, we present our formulation, the diagonal estimation for the normal operator in the curvelet domain. Following that, we summarize our algorithm. Finally, we analyze the merit of our method on a series of examples with various complexity including the BP synthetic data set (Billette and Brandsberg-Dahl, 2005).

METHODOLOGY

Ideally, the data used before the migration are primary only (no multiples), which is mathematically described as

$$\mathbf{d} = \mathbf{Km}, \quad (1)$$

where \mathbf{d} is the data; \mathbf{K} is the linearized Born scattering operator, which is also called the demigration operator; and \mathbf{m} is the reflectivity. Theoretically, migration is the adjoint of the scattering operator so that when migration is applied to data we have

$$\mathbf{m}_{\text{mig}} = \mathbf{K}^T \mathbf{d} = \mathbf{K}^T \mathbf{Km}, \quad (2)$$

where \mathbf{K}^T is the transpose of \mathbf{K} and the superscript T means transpose. The term $\mathbf{K}^T \mathbf{K}$ is the normal operator, which is also called the Hessian matrix in seismic imaging. To estimate \mathbf{m} , we need to invert this operator. In image-to-image-based methods (Rickett, 2003;

Guitton, 2004; Plessix and Mulder, 2004; Herrmann et al., 2008; Symes, 2008), the migrated image is once again remigrated, which means demigration, followed by migration (i.e., $\mathbf{m}_{\text{remig}} = \mathbf{K}^T \mathbf{Km}_{\text{mig}}$). Subsequently, using pairs of migrated and remigrated images, an approximation for the inverse of the normal operator can be found. Mathematically, the estimation for the inverse of the normal operator can be written as

$$\mathbf{m}_{\text{mig}} = (\mathbf{K}^T \mathbf{K}) f^{-1} \mathbf{m}_{\text{remig}}, \quad (3)$$

$$= \mathbf{S}^\dagger \mathbf{WSm}_{\text{remig}}, \quad (4)$$

with \mathbf{m}_{mig} being the migrated image, $\mathbf{m}_{\text{remig}}$ the remigrated image (i.e., $\mathbf{m}_{\text{remig}} = \mathbf{K}^T \mathbf{Km}_{\text{mig}}$), \mathbf{K} the demigration operator, and \mathbf{K}^T the migration operator. The approximation consists of transforming (by \mathbf{S} , a linear transformation) the remigrated image, followed by a scaling with a positive diagonal matrix (\mathbf{W}), an inverse transform to map it back to the physical domain through the pseudoinverse of \mathbf{S} (denoted by \mathbf{S}^\dagger). The performance of the scaling methods depends on two components: first is the choice of the appropriate domain for the scaling (i.e., the matrix \mathbf{S}) and the second is the calculation of the filter coefficients, i.e., the diagonal of \mathbf{W} , from the migrated image and remigrated image.

Rickett (2003) uses the scaling method first proposed by Claerbout and Nichols (1994), applies the identity basis ($\mathbf{S} = \mathbf{Id}$ with \mathbf{Id} as the identity matrix), and calculates the filter coefficients by element-wise division of images. Aside from possible instability in this division, Rickett (2003) does not apply the appropriate preconditioning to the migration operator to be sure that operator is of zero order (see, e.g., Herrmann et al., 2008; Symes, 2008). This may lead to inaccuracies in the region of the image where there are phase changes due to the nature of the operator (see, e.g., Herrmann et al., 2008). Guitton (2004) improves this technique by applying scaling in a domain spanned by a filter bank. This approach allows him to treat dips locally and to impose smoothness of the filter coefficients. However, this approach does not correct for the order of the migration operator. More recently, Symes (2008) introduces a scaling approach that corrects for the order of the normal operator by filtering the migrated and demigrated images with a fractional inverse Laplacian, followed by estimation of the physical-domain scaling using bicubic splines. He also imposes smoothness of the scaling coefficients. However, this approach assumes the existence of a well-defined dip in the migrated image because splines do not capture any dip information in the approximation. In the high-frequency limit, the scattering operator and the normal operator can, under certain conditions on the medium and ray geometry, be considered as Fourier integral operators (FIOs) (Ten-Kroode et al., 1998). In two dimensions ($d = 2$), the scattering operator \mathbf{K} and its adjoint, the migration operator \mathbf{K}^T , can be considered as FIOs of order 1/4, whereas the leading behavior for their composition, the normal operator, corresponds to an order-one invertible elliptic pseudodifferential operator (PsDO). To make this PsDO amenable to an approximation by curvelets, these operators should be made zero order by composing the data side with a 1/2-order fractional integration along the time coordinate, i.e., $d \rightarrow (\partial/\partial t)^{-\frac{1}{2}} d$. Alternatively, we can half-integrate the source wavelet along the time coordinate.

CURVELET-DOMAIN DIAGONAL APPROXIMATION OF THE NORMAL OPERATOR

A 2D curvelet ϕ_μ is defined by its index $\mu = (j, k, \theta)$ with $j = 0, 1, 2, \dots$ being the scale index, $\theta = 0, 1, \dots, 2^{\lfloor j/2 \rfloor} - 1$ the orientation index ($\lfloor x \rfloor$ is the lower integer part of x), and the location index $k = (x, z)$. Figure 1a and 1b shows an example of different curvelets with different scaling, orientation, and locations and their corresponding Fourier spectra, respectively. An important property of curvelets is that the action of the normal operator (i.e., $\Psi = \mathbf{K}^T \mathbf{K}$) on a curvelet ϕ_μ is approximately mapped into the same curvelet within a scalar. Mathematically, we can derive the following approximation:

$$\Psi\phi_\mu \approx d_\mu \phi_\mu, \quad (5)$$

with d_μ being a positive scalar multiplier dependent on the index $\mu \in M$, with M being the index set. The \approx symbol denotes “approximated by.” In Herrmann et al. (2008), we theoretically and empirically show this behavior by studying the behavior of curvelets at different scales, angles, and locations after applying the normal operator. In addition, we prove a theorem that states that the above approximation (see equation 5) becomes more accurate at the finer scales (i.e., at higher spatial frequencies).

Approximation formulation

Equation 5 suggests that curvelets are similar to eigenvectors of the normal operator. Therefore, we suggest curvelets as quasieigenvectors and form a quasieigenvalue decomposition for the normal operator. This decomposition is similar to wavelet-vaguelette decomposition proposed by Donoho (1995) and Herrmann et al. (2008),

$$\Psi\phi_\mu \approx \mathbf{C}^T \mathbf{P}_\Psi \mathbf{C}\phi_\mu, \quad (6)$$

where \mathbf{C} and \mathbf{C}^T are the curvelet transform and its adjoint (Candes et al., 2006) and \mathbf{P}_Ψ is a diagonal scaling matrix with elements of d_μ in equation 5. Because curvelets are tight frames $\mathbf{C}^T \mathbf{C} = \mathbf{I}$, with \mathbf{I} as the identity or unit matrix, assuming near unitary we can safely assume that a similar approximation holds for the inverse of the normal operator with

$$\Psi^{-1}\phi_\mu \approx \mathbf{C}^T \mathbf{P}_\Psi^{-1} \mathbf{C}\phi_\mu. \quad (7)$$

As we mentioned, our method is based on an image-to-image fitting scheme. Comparing equation 7 with equation 3 results in $\mathbf{W} = \mathbf{P}_\Psi^{-1}$; hence, we have the following form:

$$\mathbf{m}_{\text{mig}} \approx \mathbf{C}^T \mathbf{W} \mathbf{C} \mathbf{m}_{\text{remig}} \mapsto \mathbf{m}_{\text{mig}} \approx \mathbf{C}^T \text{diag}(\mathbf{v}) \mathbf{w}, \quad (8)$$

with $\mathbf{v} = \mathbf{C} \mathbf{m}_{\text{remig}}$ and \mathbf{w} representing the diagonal elements of \mathbf{W} (i.e., $\mathbf{W} = \text{diag}(\mathbf{w})$). This method aims to find a curvelet-domain diagonal scaling approximation (i.e., estimating \mathbf{w} in equation 8) that resembles the action of the inverse of the normal operator on the reference vector. Because the curvelet transform is redundant, equation 8 is an underdetermined system of equations yielding nonunique solutions. To find a unique solution to this diagonal approximation problem, we exploit additional properties of the normal operator. First, the normal operator is positive definite yielding

positive entries for the scaling vector \mathbf{w} . Second, the symbols of the PsDO, i.e., space and spatial frequency-dependent multipliers (in this case, curvelet coefficients) are known to be smooth for the smooth background velocity model (Stein, 1993; Stolk and De Hoop, 2006; Herrmann et al., 2008). We use these properties to formulate the diagonal approximation problem using a nonlinear least-

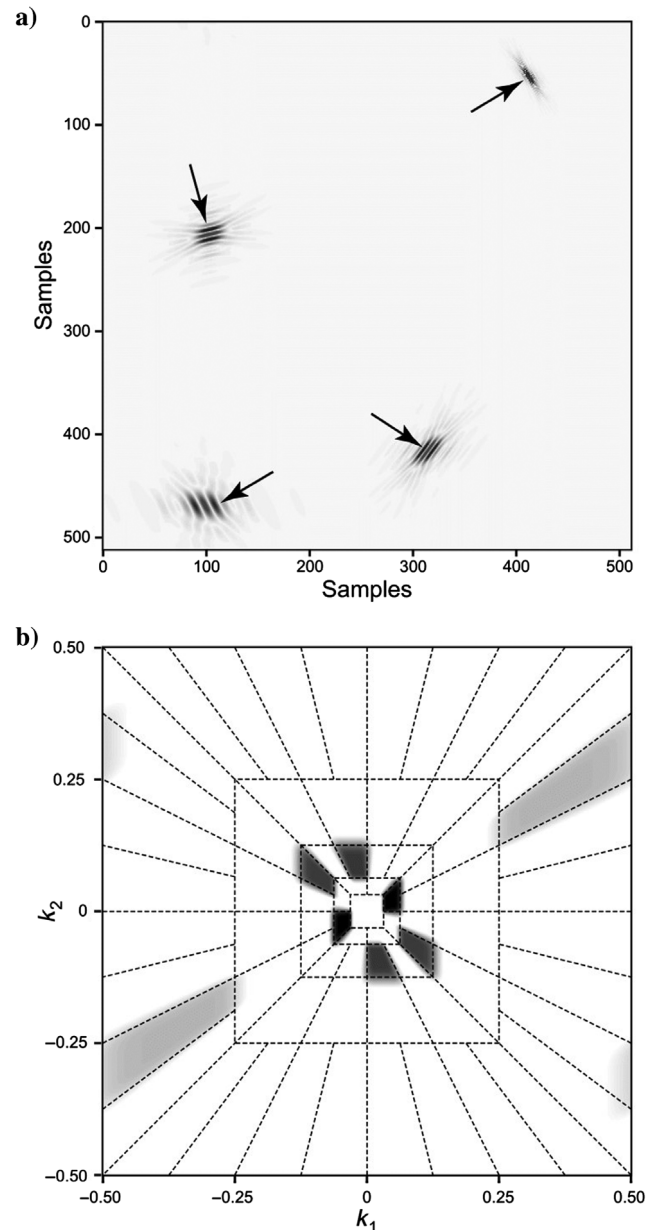


Figure 1. Spatial and frequency representation of the curvelets. (a) Four different curvelets in the spatial domain at three different scales. (b) Dyadic partitioning in the frequency domain, in which each wedge corresponds to the frequency support of a curvelet in the spatial domain. This figure illustrates the microlocal correspondence between the curvelets in the physical and Fourier domain. Curvelets are characterized by a rapid decay in the physical space and of compact support in the Fourier space. Notice the correspondence between the orientation of curvelets in the two domains. The 90° rotation is a property of the Fourier transform. Courtesy of Herrmann et al. (2008).

squares problem with enforcing positivity for the entries of the diagonal and smoothness among neighboring curvelet coefficients. The diagonal approximation reads

$$\mathbf{P}_1 : \begin{cases} \hat{\mathbf{z}} = \arg \min_{\mathbf{z}} J(\mathbf{z}) = \frac{1}{2} \|\mathbf{m}_{\text{mig}} - \mathbf{C}^T \text{diag}(\mathbf{v}) e^{\mathbf{z}}\|_{\ell_2} + \frac{1}{2} \kappa \|\mathbf{L} e^{\mathbf{z}}\|_{\ell_2}, \\ \hat{\mathbf{w}} = e^{\hat{\mathbf{z}}}, \end{cases} \quad (9)$$

where \mathbf{w} is replaced by $e^{\mathbf{z}}$ to ensure that the estimate of the diagonal elements of \mathbf{W} are all positive. We also implement the smoothness constraint on $e^{\mathbf{z}}$. In equation 9, $\mathbf{L} = [\mathbf{D}_x \quad \mathbf{D}_z \quad \mathbf{D}_{\theta}]$ is a derivative operator in the curvelet domain, penalizing the fluctuations among neighboring coefficients in $e^{\mathbf{z}}$. Matrix $\mathbf{D}_{x,z}$ contains the first-order differences at each scale in the x, z -directions, and matrix \mathbf{D}_{θ} contains the first-order difference in the angle direction. These differences are scale-dependent because curvelet partitioning of the phase space is performed in different scales. The term κ is a smoothness control parameter. The well-behaved objective function in equation 9 can be minimized by an efficient numerical optimization method. We choose to use the limited-memory Broyden-Fletcher-Goldfarb-Shanno method (see, e.g., Nocedal and Wright, 1999), knowing the gradient of the minimization functional in equation 9 as

$$\nabla_{\mathbf{z}} J(\mathbf{z}) = e^{\mathbf{z}} \cdot \text{diag}(\mathbf{v}) \mathbf{C} (\mathbf{C}^T \text{diag}(\mathbf{v}) e^{\mathbf{z}} - \mathbf{m}_{\text{mig}}) + \kappa e^{\mathbf{z}} \cdot \mathbf{L}^T \mathbf{L} e^{\mathbf{z}}, \quad (10)$$

where $\cdot \cdot \cdot$ denotes the component-wise product of the vectors.

ALGORITHMIC DETAILS

As we show below, the algorithm requires access to matrix-free implementations of the Born modeling operator and its adjoint. For our 2D example, we use operators from reverse time migration-demigration. The recovery algorithm in this paper is designed to be part of a postprocessing procedure that enhances the amplitudes of the seismic image. The algorithm consists of two main steps, namely, the calculation of the curvelet scaling coefficients via an image-to-remigrated-image matched filtering and a subsequent recovery. Our algorithm consists of the following steps:

- 1) Perform the migration and the depth correction — i.e., $\mathbf{d} \mapsto \mathbf{D}\mathbf{K}^T \mathbf{d} = \tilde{\mathbf{m}}_{\text{mig}}$, with $\tilde{\mathbf{m}}_{\text{mig}}$ as the depth-corrected migrated image and $\mathbf{D} = \text{diag}(z)$, where $z = i\Delta z$, for $i = 1:n_z$, Δz is the depth grid spacing, and n_z is the number of samples in depth. The reason for the depth correction is to boost the amplitudes of deep events in the migrated image. This ensures that after applying the normal operator on the migrated image, the deep events will be visible in the remigrated image and can contribute accordingly to the diagonal estimation.
- 2) Remigrate the migrated image — i.e., $\tilde{\mathbf{m}}_{\text{mig}} \mapsto \mathbf{K}^T \mathbf{K} \tilde{\mathbf{m}}_{\text{mig}} = \mathbf{m}_{\text{remig}}$.
- 3) Find the diagonal scaling \mathbf{W} in the curvelet domain for which $\tilde{\mathbf{m}}_{\text{mig}} \approx \mathbf{C}^T \mathbf{W} \mathbf{C} \mathbf{m}_{\text{remig}}$ by solving optimization problem \mathbf{P}_1 (see equation 9).
- 4) Construct the original image by applying the approximation to migrated image (not depth corrected) $\hat{\mathbf{m}} = \mathbf{C}^T \mathbf{W} \mathbf{C} \mathbf{m}_{\text{mig}}$.

EXAMPLES

In this section, we first show the effect of the normal operator on a curvelet with different background velocity models. Then, we show our amplitude recovery method on a series of stylized examples. We use a constant-density, two-way acoustic wave equation RTM and demigration. We apply our method to the linearized Born and full synthetic data (i.e., the solution of the nonlinear wave equation) on a model with reflectors that have conflicting dips. We conclude by testing our algorithm on the large-scale BP velocity benchmark (Billette and Brandsberg-Dahl, 2005).

Curvelet invariance under the action of the normal operator

In this section, we provide an example to show how a curvelet is changed under the action of the normal operator. In this example, we apply the normal operator on a curvelet with different types of background velocity models, i.e., constant, smoothly varying, and nonsmooth background velocity models as shown in Figure 2. The velocity model for this example is a part of the North Sea velocity model with a salt body in the middle. Figure 2a shows a curvelet that has been used as the model reflectivity, Figure 2b shows the smoothly varying velocity model obtained by low-pass filtering the hard model, and Figure 2c shows the original model without any smoothness. Figure 2d–2f shows the effect of the normal operator on the curvelet shown in Figure 2a, and Figure 2g–2i shows the Fourier-domain support of Figure 2d–2f, respectively. As can be seen from these figures, the angle, orientation, and physical location of the curvelet remain invariant under the action of the normal operator with a slight support loss in the Fourier domain from left to right, which should be expected when the background model changes from the constant to the heterogeneous model. These figures confirm the theorem that the curvelet remain almost invariant under the action of the normal operator with a moderate degree of accuracy.

Conflicting-dip velocity model

We generate two sets of synthetic data. First, we use the linearized Born scattering operator (i.e., $\mathbf{d} = \mathbf{K}\mathbf{m}$ with \mathbf{m} being the reflectivity and \mathbf{K} being the scattering operator) and an acoustic wave propagator to generate the synthetic data set. Second, we produce data by solving the acoustic wave equation for the challenging model (Figure 3).

Linearized Born scattering data set

This example, which is shown in Figure 3a, uses a land acquisition with 32 shots between 0 and 2048 m at a 64 m spacing and 512 receivers per shot at a 4 m interval with offsets between 0 and 2048 m. To generate the linearized Born data set, we smooth this velocity model as shown in Figure 3b, and we use the difference between the smoothed and the original velocity as the reflectivity shown in Figure 3c. We choose this velocity model to demonstrate the ability of our algorithm to handle conflicting dips. As reported in the literature, situations involving no unique dips may result in erroneous amplitude correction (Symes, 2008).

Figure 4 summarizes our approximation of the normal operator with curvelet-domain scaling. We choose the reflectivity in Figure 3c and apply the scattering operator to generate the data set

(i.e., $\mathbf{d} = \mathbf{Km}$). We use the smoothed velocity model shown in Figure 3b as the background velocity for the scattering operator. The migrated result with the same background velocity model on linearized Born data is included in Figure 4a after applying the aforementioned depth correction. Notice the amplitude effects, which are more pronounced after the modeling and remigration of this image as shown in Figure 4b. These two images serve as the input to our curvelet scaling coefficient estimation. Applying curvelet-domain scaling to the reference image yields as good an approximation to the action of the normal operator as can be seen in Figure 4c.

To illustrate the importance of imposing the curvelet-domain smoothness during the scale coefficient estimation, we conduct two experiments, one without ($\kappa = 0$) and one with a smoothing regularization ($\kappa = 0.1$, which was chosen empirically and used to generate the example in Figure 4). From Figure 5, it is clear that the scale-coefficient estimation becomes biased toward the reference vector. This figure shows the curvelet transform of the reference vector (Figure 5a), a diagonal estimation without smoothness (Figure 5b) and with smoothness constraints (Figure 5c). As we can see, the curvelet coefficients for the reference image vary with scales that become finer when moving from the center outward. The angular wedges are roughly localized in positions that correspond to the angle of the curvelets. In other words, if this angle is close to the dip of the event, the curvelet coefficient will be large. This domain nicely decomposes the reflectivity into different scales and angles. This explains the success of curvelets in representing images with wavefronts and justifies our choice of this domain

to do the scaling. However, as Figure 5a and 5b indicates, it is important to note how to estimate the scaling coefficients. Contrary to the reflectivity itself, with its wavefronts and hence localized features in the curvelet space, the scaling has to be smooth for smooth background velocity models for which the symbols of Ψ are smooth (Herrmann et al., 2008). Comparing Figure 5b and 5c, we see large coefficients in the top row that correspond to curvelets with the wrong angles in Figure 5b, whereas these coefficients do not exist in the diagonal estimation with smoothing (Figure 5c). The final result of our amplitude recovery for this diagonal is included in Figure 6. As one can see, the amplitudes are restored reasonably well even in the areas of conflicting dip in the reflectivity.

Synthetic data set

The velocity model in Figure 3a is also used to generate nonlinear synthetic data up to 60 Hz using a finite-difference constant-density acoustic code for the same land acquisition configuration. After applying a half-time integration and removing the direct waves from the data set, we follow the same process as mentioned in the previous section. As we can see from Figure 7, our recovery method also performs well on full synthetic data.

Large-scale synthetic example

The next example is based on the BP salt model (Billette and Brandsberg-Dahl, 2005). The BP model has been designed to

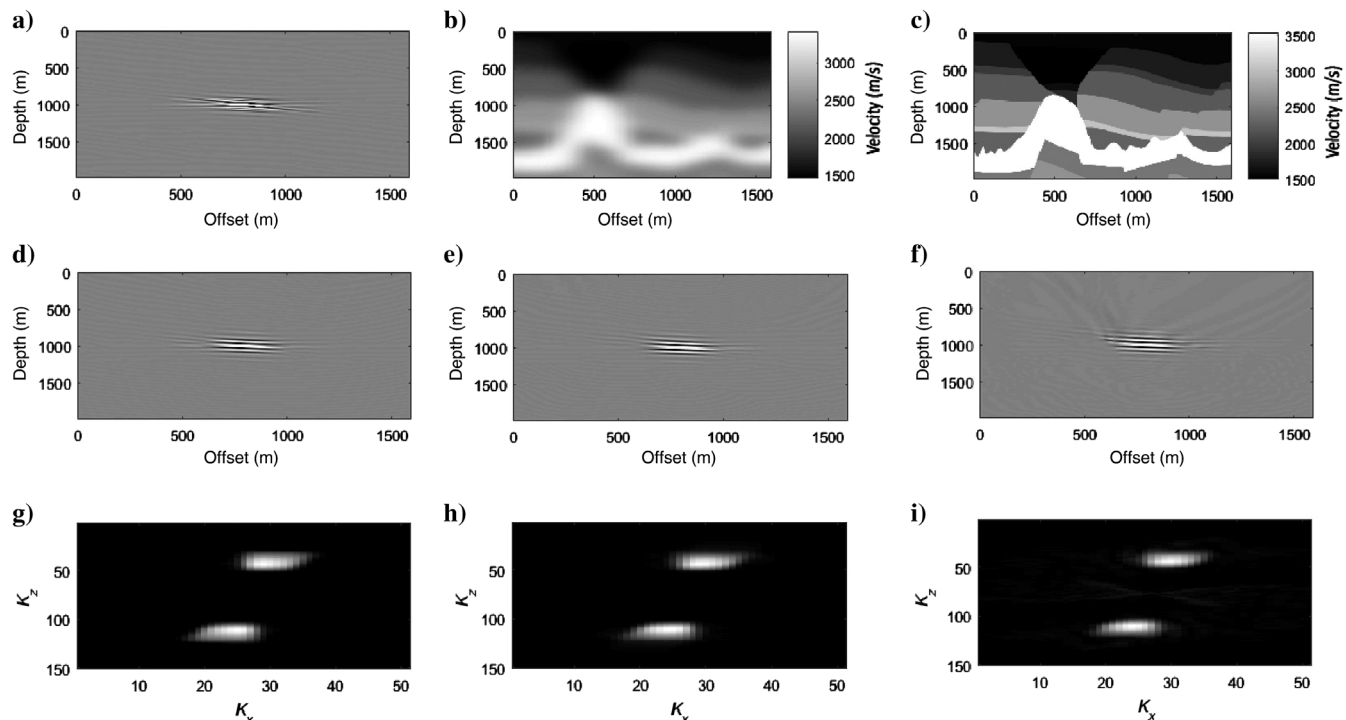


Figure 2. Action of the normal operator on a curvelet. (a) A curvelet as reflectivity, (b) smooth North Sea model, (c) hard North Sea model, (d) action of the normal operator on a curvelet with the constant velocity model (2500 m/s), (e) action of the normal operator on a curvelet with the smooth velocity model shown in (b), (f) action of the normal operator on a curvelet with the hard velocity model shown in (c), (g) Fourier domain representation of (d), (h) Fourier domain representation of (e), and (i) Fourier domain representation of (f).

exhibit illumination problems due to the complex salt shape, with a tooth-shaped salt top found in the area (Figure 8a). The data set was calculated using finite-difference modeling code with a free-surface boundary condition that generated free-surface multiples.

The data are generated with a streamer configuration, using a 15 km streamer with a 12.5 m group interval and a 50 m shot interval and 0 m minimum offset, and are recorded for 14 s with a 6 ms sampling interval. The dominant frequency is 27 Hz, and data can be whitened up to 54 Hz. The low-cut frequency is 3 Hz, and the wavelet is causal and has not been zero phased. In this example, a total of 1340 shots were generated, each with 1201 receivers.

The center part of the model (the tooth part) is exclusively extra salt, and it is meant to represent a geologic setting with shallow

gas and localized shallow anomalies (Figure 8b). However, because of the lensing effect, this part turned out to be extremely difficult to estimate for imaging methods. The geology in this part of the model is common in areas such as the Caspian Sea, offshore Trinidad, and in the North Sea. The velocity field has significant variations in the long-wavelength component and several low-velocity anomalies in the shallow section. The size, shape, and velocity of the anomalies

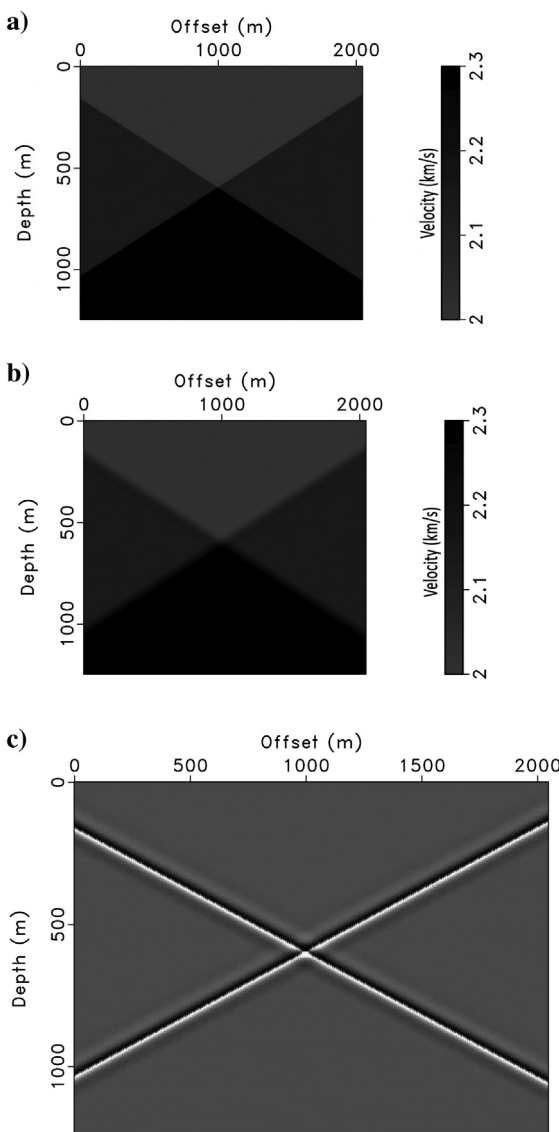


Figure 3. Conflicting dip velocity model and reflectivity. (a) Velocity model, (b) smooth velocity model used to generate our example, and (c) reflectivity generated by subtracting the smooth velocity model from the original one.

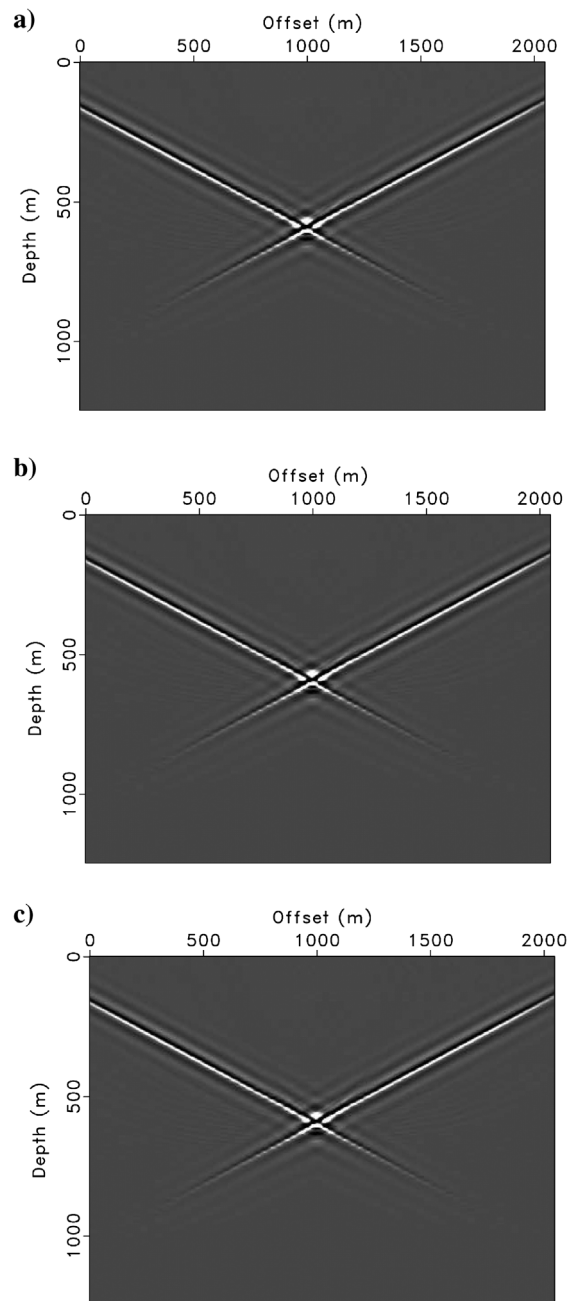


Figure 4. Example of amplitude recovery using the linearized Born modeling data set. (a) Reference image (depth-corrected migrated image), (b) the action of the normal operator on the reference image (i.e., $\Psi\mathbf{r}$), and (c) the approximate normal operator on the reference image (i.e., $\mathbf{C}^T \mathbf{D}_\Psi \mathbf{C}\mathbf{r}$), with an approximation error of 3.71%.

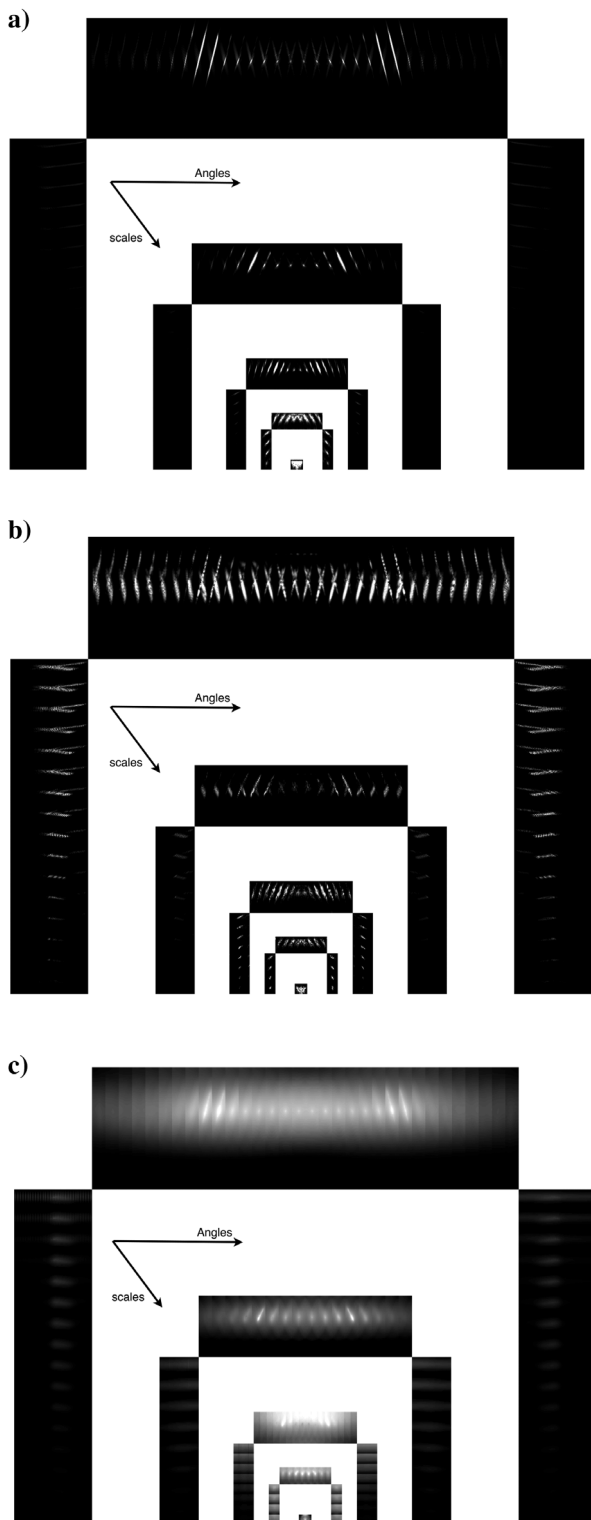


Figure 5. Curvelet-domain representation of the curvelet vector obtained from CurveLab. (a) Reference vector, (b) scaling coefficients without smoothing constraints, and (c) scaling coefficients with smoothing constraints. The different subimages represent the curvelet coefficients at different scales (coarsest in the center) and different angles.

are variable (Billette and Brandsberg-Dahl, 2005). We focus in that area of the model and show that our recovery method enhances this part of the model. We perform some pre-/postprocessing before/after migrating the data. For this purpose, the first step is to remove free surface multiples using the surface-related multiple elimination method Berkout and Verschuur (1997) and mute the direct wave in the data set. The next step is to remove the dipping wave by band-pass filtering the migrated image and to correct the migrated image with an illumination map.

Figures 9, 10, 11, and 12 show the application of our method on this model. Figure 9a shows the migrated image. We use this image as the reference vector for the amplitude recovery method discussed in the “Algorithmic details” section. Figure 9b shows the enhanced image that is the result of our proposed amplitude recovery method. Note the improvement of the enhanced image compared to the migrated image especially in the locations marked by the arrowheads. As the arrowheads indicate, improvements are visible on the top of the salt with less ringing effect and more continuity along the top salt reflector, under the salt tooth with a boost in the reflector energy and better visibility under the salt tooth, and under the velocity lens in the middle of the model with better energy focusing and reflector visibility.

To show that our methodology is not simply a boost in the amplitude in the enhanced image, we set up the following experiment.

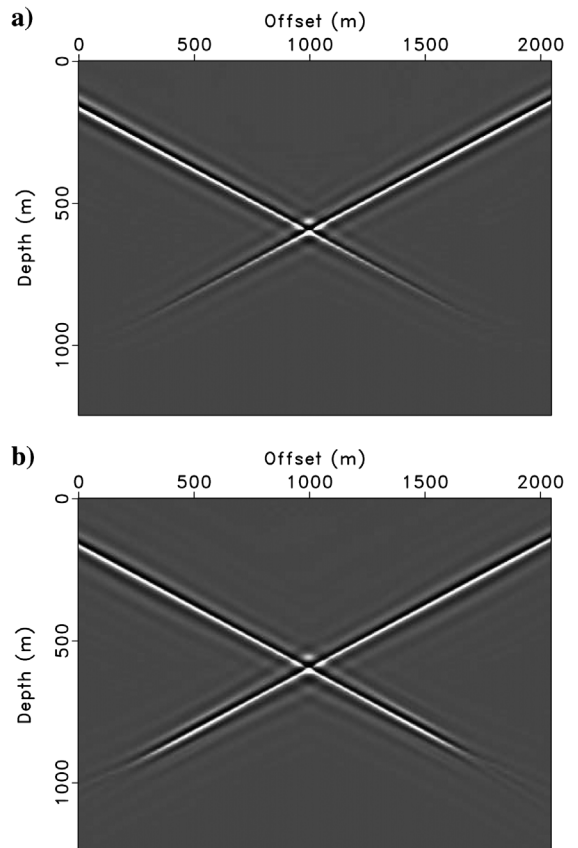


Figure 6. Example of amplitude recovery using the linearized Born modeling data set. (a) Reference image (the depth-corrected migrated image) and (b) enhanced image. Notice the enhancement along the deeper part of the reflectors.

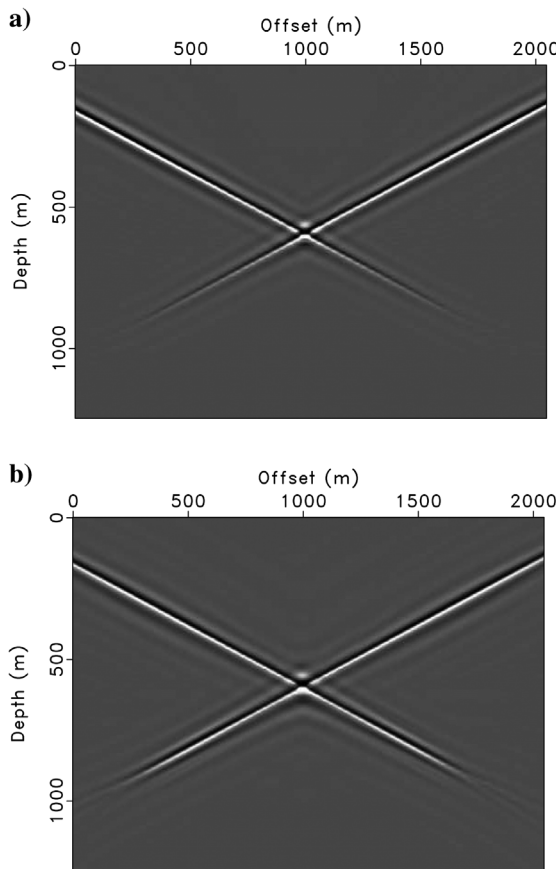


Figure 7. Example of amplitude recovery using acoustic wave propagation data set (not linearized). (a) Reference image (the depth-corrected migrated image) and (b) enhanced image.

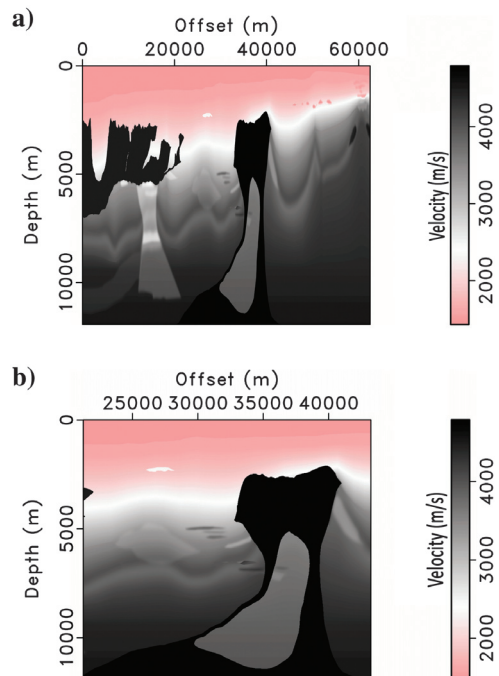


Figure 8. The BP velocity model. (a) The full model and (b) the tooth part of the BP model, area of interest.

Figure 10 shows the vertical derivative in the BP density model. This figure can be considered as the benchmark to compare how well our recovery method performs. Considering the fact that the seismic image is ideally a representative of the perturbation in the reflectivity (not the reflectivity itself) and in the BP model most

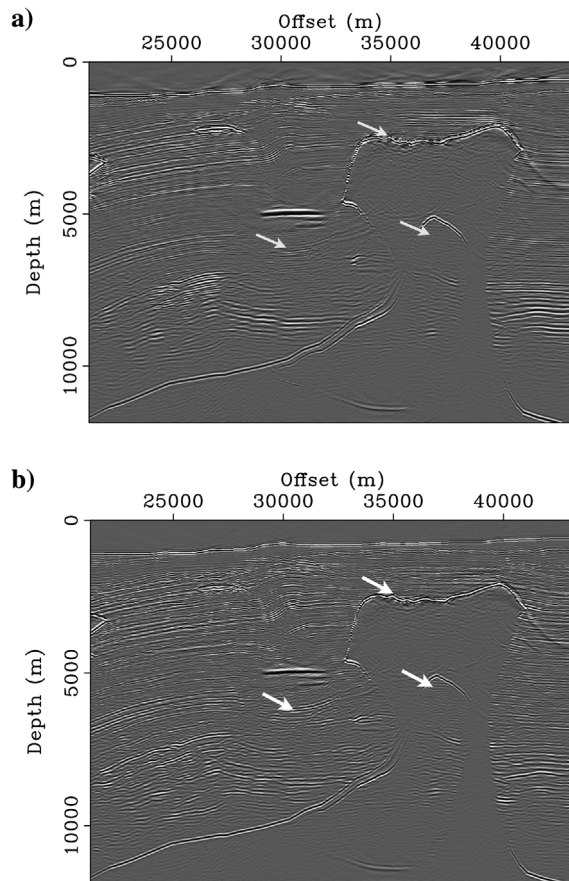


Figure 9. Our recovery result: (a) BP migrated image (illumination corrected) and (b) BP enhanced image.

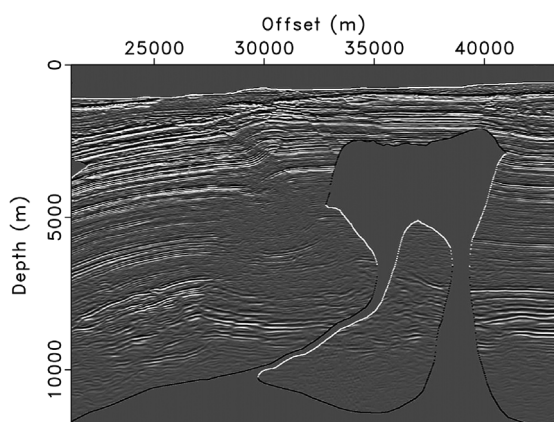


Figure 10. Differentiated density model.

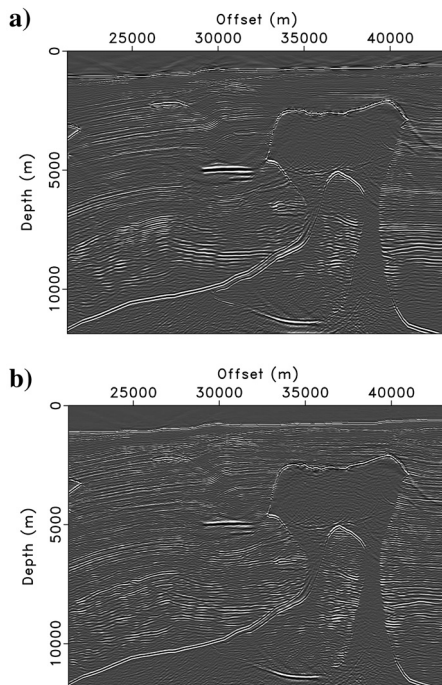


Figure 11. Result of AGC on the (a) migrated image and (b) enhanced image.

variation occurs in the density model instead of velocity (Billette and Brandsberg-Dahl, 2005), Figure 10 shows a good benchmark to compare with our final result. The closer the enhanced image is to the benchmark image means that our recovery method has a better performance.

To have an unbiased comparison between the migrated image and the enhanced image, we apply automatic gain control (AGC) to both images. Figure 11 shows the result of AGC on the migrated and the enhanced image.

Figures 12 and 13 display magnifications of two different areas shown in the images in Figure 11 to show how well our method performs. Figure 12a and 12b shows the migrated and the enhanced image around the potential reservoir zone, under the velocity lens, located at approximately (5000, 30,000) m, respectively. Comparing Figure 12b, the enhanced image, and Figure 12a, the migrated image, with the benchmark density model in Figure 12d, it is visible that the enhanced image could capture most density variations that exist in the density model with reasonably good amplitude preservation, whereas in the migrated image some important regions are faded away specially under the velocity lens.

Figure 13a and 13b shows the migrated and the enhanced image under the tooth-shape salt flank, respectively. Compared with the density model, shown in Figure 13d, we observe promising amplitude recovery results and noticeable amplitude recovery in the enhanced image.

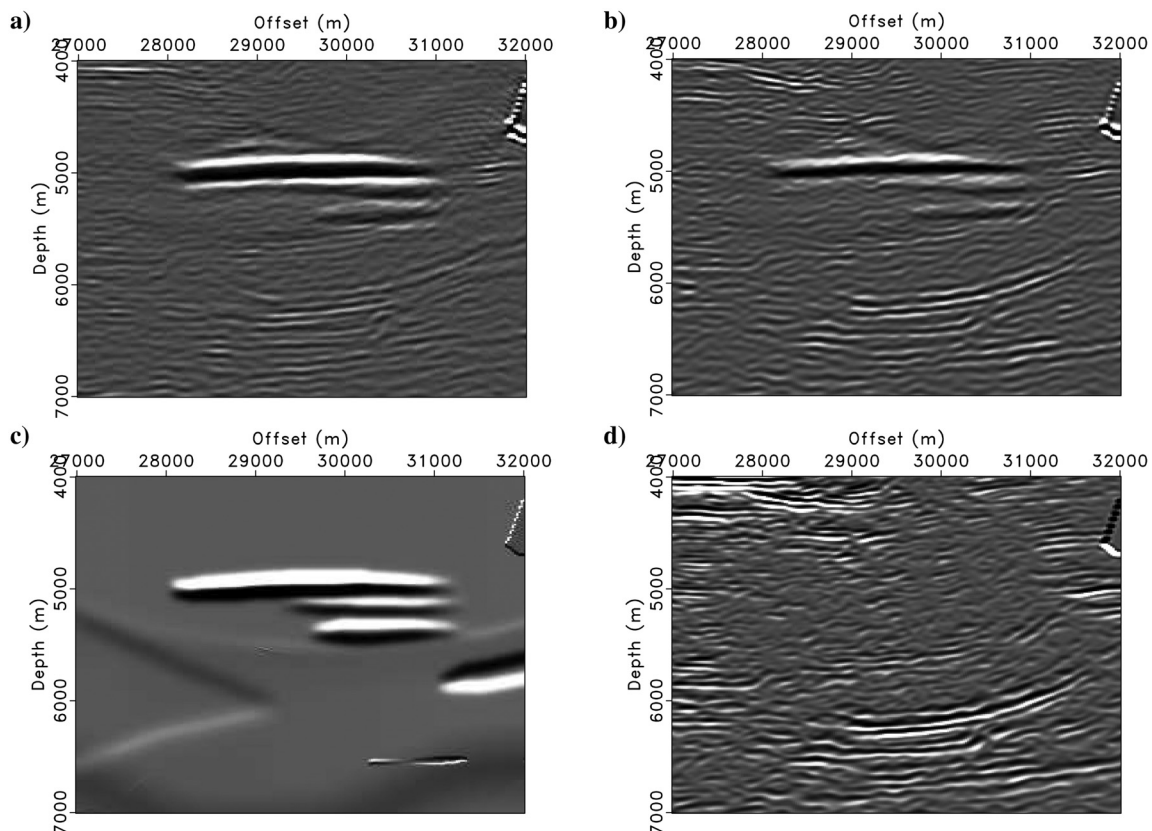


Figure 12. Comparison between the migrated and the enhanced image in potential reservoir zones. (a) Migrated, (b) enhanced, (c) velocity differentiated along the vertical access, and (d) density differentiated along the vertical access.

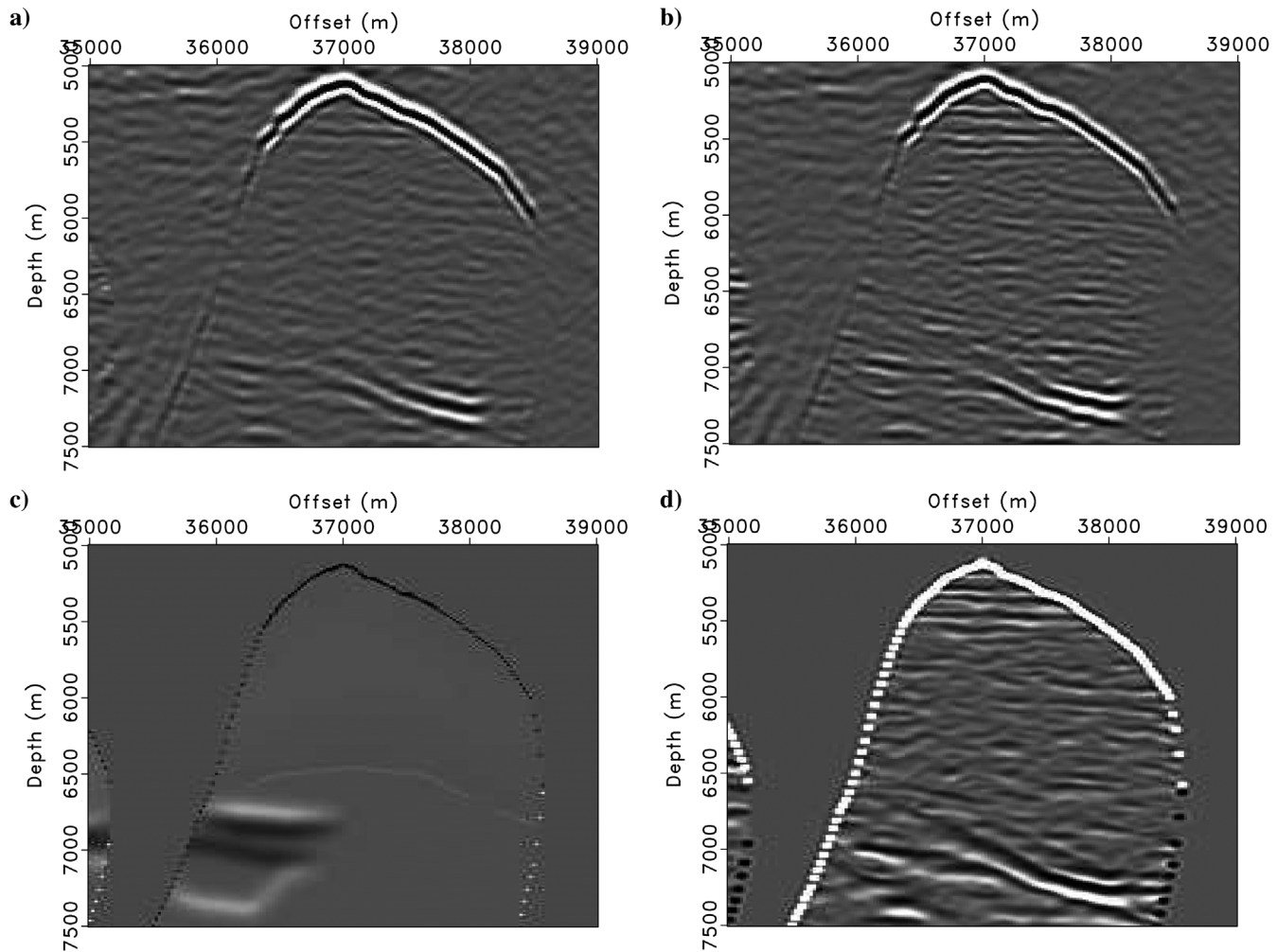


Figure 13. Comparison between the migrated and enhanced image in the undersalt zone. (a) Migrated, (b) enhanced, (c) velocity differentiated along the vertical access, and (d) density differentiated along the vertical access.

CONCLUSION

The migration section is an inaccurate image of the geologic reflectivity distribution if it is imaged incorrectly. With a coarsely sampled and narrow distribution of sources and receivers, the migration output introduces inaccuracy into the amplitude of the reflectors. Furthermore, migration is not the exact inverse of the forward-modeling operator, so the migration image is only a rough approximation of the reflectivity image.

To mitigate these effects, we present a fast and robust approach to approximation of the normal operator and use it to recover the amplitudes in the migrated image. We formulate the approximation of the normal operator as an eigenvalue-like decomposition with curvelets as eigenvectors. Our proposed method is faster than other methods because our method evaluates the normal operator only once. The method presented in this paper comprises the two important properties of the curvelet transform, namely, the smoothness of its coefficient and the invariance of its elements under the action of the normal operator. This combination allows us to formulate a stable recovery method for seismic amplitudes.

Compared with other approaches for migration amplitude recovery, some noteworthy improvements in this method are, first, speeding up the calculation of the normal operator by diagonalizing it in the curvelet domain, second, designing an efficient approximation that takes into account a laterally variant velocity model and steep reflectors, third, replacing the ad hoc or trial-and-error estimation of the migration amplitude with a method that has a more theoretical and practical background, and, fourth, bringing the amplitude correction problem within the context of stable recovery.

The results of applying our method on synthetic data suggest that our migration amplitude recovery can be useful in eliminating migration artifacts and in the seismic image. The recovered images show the partial elimination of noise, improved spatial resolution, and enhanced reflectivity amplitude.

DATA AND MATERIALS AVAILABILITY

Data associated with this research are available and can be obtained by contacting the corresponding author.

APPENDIX A REVERSE TIME WAVE EQUATION MIGRATION

Most migration operators are defined to be the adjoint of what is called the scattering operator. This assumption is also true for RTM.

Single scattering

The causal acoustic Green's function $G(\mathbf{x}, t; \mathbf{x}_s), \mathbf{x} \in \mathbf{R}^3$ for a point source at $\mathbf{x} = \mathbf{x}_s$ is the solution of

$$\frac{1}{v^2(\mathbf{x})} \frac{\partial^2 G}{\partial t^2}(\mathbf{x}, t; \mathbf{x}_s) - \nabla_x^2 G(\mathbf{x}, t; \mathbf{x}_s) = \delta(\mathbf{x} - \mathbf{x}_s)\delta(t), \quad (\text{A-1})$$

with $G = 0$, $t < 0$, and v is the acoustic wave velocity field.

Denote by $m(\mathbf{x}) = \delta v(\mathbf{x})/v(\mathbf{x})$ a relative perturbation of the velocity field. Then, linearization of the wave equation yields for the corresponding perturbation of the Green's function

$$\begin{aligned} & \frac{1}{v^2(\mathbf{x})} \frac{\partial^2 \delta G}{\partial t^2}(\mathbf{x}, t; \mathbf{x}_s) - \nabla_x^2 \delta G(\mathbf{x}, t; \mathbf{x}_s) \\ &= \frac{2m(\mathbf{x})}{v^2(\mathbf{x})} \frac{\partial^2}{\partial t^2} G(\mathbf{x}, t; \mathbf{x}_s), \end{aligned} \quad (\text{A-2})$$

whose solution has the integral representation, at the source and receiver points $\mathbf{x}_r, \mathbf{x}_s$, respectively, as

$$\begin{aligned} \delta G(\mathbf{x}_r, t; \mathbf{x}_s) &= \frac{\partial^2}{\partial t^2} \int dx \int d\tau \frac{2m(\mathbf{x})}{v^2(\mathbf{x})} G(\mathbf{x}, t - \tau; \mathbf{x}_r) \\ &\quad \times G(\mathbf{x}, \tau; \mathbf{x}_s). \end{aligned} \quad (\text{A-3})$$

Shot-geophone modeling and migration

The single-scattered wavefield is the time convolution of G with a source wavelet. The main concern of this paper is the kinematic relationships between the data and the image; thus, we ignore the filtering effect of the source functional and replace it with the delta function. This replacement of the source by an impulse does not violate any of our assumptions regarding the adjoint-state method, thus the Born modeling operator $K[v]$ is

$$K[v]m(\mathbf{x}) = \delta G(\mathbf{x}_r, t; \mathbf{x}_s). \quad (\text{A-4})$$

The crux of our amplitude recovery method relies on the shot-geophone migration operator to be the adjoint of the shot-geophone modeling operator. The derivation of the adjoint reverse time implementation is a minor variation on the usual implementation of RTM (the “adjoint state method”; see, e.g., Lailly and Bednar, 1983; Whitmore, 1983; Tarantola, 1984; Yoon et al., 2003; Symes, 2007). The result is

$$\begin{aligned} K^*[v]d(\mathbf{x}_r, t; \mathbf{x}_s) &= \hat{m}(\mathbf{x}) = - \int dx_s \int_0^T dt 2v(\mathbf{x}) \\ &\quad \times q(\mathbf{x}, t; \mathbf{x}_s) \frac{\partial^2 G}{\partial t^2}(\mathbf{x}, t; \mathbf{x}_s), \end{aligned} \quad (\text{A-5})$$

where the adjoint state or backpropagated field $q(\mathbf{x}, t; \mathbf{x}_s)$ satisfies $q = 0$, $t > T$, and

$$\begin{aligned} & \frac{1}{v^2(\mathbf{x})} \frac{\partial^2 q}{\partial t^2}(\mathbf{x}, t; \mathbf{x}_s) - \nabla_x^2 q(\mathbf{x}, t; \mathbf{x}_s) \\ &= \int dx_r d(\mathbf{x}_r, t; \mathbf{x}_s) \delta(\mathbf{x} - \mathbf{x}_r). \end{aligned} \quad (\text{A-6})$$

The migration operator defined by the above equations is the RTM operator. Symes et al. (2003) show that the migration operator, which is defined in equations A-5 and A-6, is the adjoint of the modeling operator defined in equation A-3. The RTM that is used for this work is the adjoint of the modeling operator and is properly tested in the discrete sense. By having the migration and modeling operators properly set, we can proceed with our amplitude-recovery method.

REFERENCES

- Berkhout, A., and D. Verschuur, 1997, Adaptive surface-related multiple elimination: Geophysics, **62**, 1586–1595, doi: [10.1190/1.1444261](https://doi.org/10.1190/1.1444261).
- Billette, F. J., and S. Brandsberg-Dahl, 2005, The 2004 BP velocity benchmark: 67th Annual International Conference and Exhibition, EAGE, Extended Abstracts, cp-1, doi: [10.3997/2214-4609-pdb.1.B035](https://doi.org/10.3997/2214-4609-pdb.1.B035).
- Candes, E., L. Demanet, D. Donoho, and L. Ying, 2006, Fast discrete curvelet transforms: SIAM Multiscale Modeling & Simulation, **5**, 861–899, doi: [10.1137/05064182X](https://doi.org/10.1137/05064182X).
- Chattopadhyay, S., and G. A. McMechan, 2008, Imaging conditions for pre-stack reverse-time migration: Geophysics, **73**, no. 3, S81–S89, doi: [10.1190/1.2903822](https://doi.org/10.1190/1.2903822).
- Chauris, H., and E. Cocher, 2017, From migration to inversion velocity analysis: Geophysics, **82**, no. 3, S207–S223, doi: [10.1190/geo2016-0359.1](https://doi.org/10.1190/geo2016-0359.1).
- Claerbout, J., 1992, Earth soundings analysis, processing versus inversion: Blackwell Scientific Publications 6.
- Claerbout, J., and D. Nichols, 1994, Spectral preconditioning: Technical Report 82, Stanford Exploration Project, Stanford University, 82, 1–187.
- Costa, J., F. S. Neto, M. Alcantara, J. Schleicher, and A. Novais, 2009, Obliquity-correction imaging condition for reverse time migration: Geophysics, **74**, no. 3, S57–S66, doi: [10.1190/1.3110589](https://doi.org/10.1190/1.3110589).
- da Silva Neto, F. A., J. C. Costa, J. Schleicher, and A. Novais, 2011, 2.5-D reverse-time migration: Geophysics, **76**, no. 4, S143–S149, doi: [10.1190/1.3571272](https://doi.org/10.1190/1.3571272).
- Donoho, D., 1995, Nonlinear solution of linear inverse problems by wavelet-vaguelette decomposition: Applied and Computational Harmonic Analysis, **2**, 101–126, doi: [10.1006acha.1995.1008](https://doi.org/10.1006acha.1995.1008).
- Gray, S., 1997, True amplitude seismic migration: A comparison of three approaches: Geophysics, **62**, 929–936, doi: [10.1190/1.1444200](https://doi.org/10.1190/1.1444200).
- Guitton, A., 2004, Amplitude and kinematic corrections of migrated images for nonunitary imaging operators: Geophysics, **69**, 1017–1024, doi: [10.1190/1.1778244](https://doi.org/10.1190/1.1778244).
- Herrmann, F., P. Moghaddam, and C. Stolk, 2008, Sparsity- and continuity-promoting seismic image recovery with curvelet frames: Applied and Computational Harmonic Analysis, **24**, 150–173, doi: [10.1016/j.acha.2007.06.007](https://doi.org/10.1016/j.acha.2007.06.007).
- Herrmann, F. J., and X. Li, 2012, Efficient least-squares imaging with sparsity promotion and compressive sensing: Geophysical Prospecting, **60**, 696–712, doi: [10.1111/j.1365-2478.2011.01041.x](https://doi.org/10.1111/j.1365-2478.2011.01041.x).
- Hou, J., and W. W. Symes, 2015, An approximate inverse to the extended born modeling operator: Geophysics, **80**, no. 6, R331–R349, doi: [10.1190/geo2014-0592.1](https://doi.org/10.1190/geo2014-0592.1).
- Kuel, H., and M. Sacchi, 2003, Least-squares wave-equation migration for AVP/AVA inversion: Geophysics, **68**, 262–273, doi: [10.1190/1.1543212](https://doi.org/10.1190/1.1543212).
- Lailly, P., and J. Bednar, 1983, The seismic inverse problem as a sequence of before stack migrations: Conference on Inverse Scattering: Theory and Application, 206–220.
- Li, Y., and H. Chauris, 2018, Coupling direct inversion to common-shot image-domain velocity analysis: Geophysics, **83**, no. 5, R497–R514, doi: [10.1190/geo2017-0825.1](https://doi.org/10.1190/geo2017-0825.1).
- Liu, Q., and D. Peter, 2018, One-step data-domain least-squares reverse time migration: Geophysics, **83**, no. 4, R361–R368, doi: [10.1190/geo2017-0622.1](https://doi.org/10.1190/geo2017-0622.1).
- Lu, S., X. Li, A. Valenciano, N. Chemingui, and C. Cheng, 2017, Least-squares wave-equation migration for broadband imaging: 79th Annual International Conference and Exhibition, EAGE, Extended Abstracts, 1–5.
- Mulder, W., and R.-E. Plessix, 2004, A comparison between one-way and two-way wave equation migration: Geophysics, **69**, 1491–1504, doi: [10.1190/1.1836822](https://doi.org/10.1190/1.1836822).
- Nocedal, J., and W. Wright, 1999, Numerical optimization: Springer Verlag.

- Plessix, R., and W. Mulder, 2004, Frequency-domain finite-difference amplitude-preserving migration: *Geophysical Journal International*, **157**, 975–987, doi: [10.1111/j.1365-246X.2004.02282.x](https://doi.org/10.1111/j.1365-246X.2004.02282.x).
- Rickett, J., 2003, Illumination-based normalization for wave-equation depth migration: *Geophysics*, **68**, 1371–1379, doi: [10.1190/1.1598130](https://doi.org/10.1190/1.1598130).
- Schleicher, J., J. C. Costa, and A. Novais, 2008, A comparison of imaging conditions for wave-equation shot-profile migration: *Geophysics*, **73**, no. 6, S219–S227, doi: [10.1190/1.2976776](https://doi.org/10.1190/1.2976776).
- Stein, E., 1993, Harmonic analysis: Vanderbilt University Press.
- Stolk, C., and M. De-Hoop, 2006, Seismic inverse scattering in the downward continuation approach: *Wave Motion*, **43**, 579–598, doi: [10.1016/j.wavemoti.2006.05.003](https://doi.org/10.1016/j.wavemoti.2006.05.003).
- Symes, W. W., 2007, Reverse time migration with optimal checkpointing: *Geophysics*, **72**, no. 5, SM213–SM221, doi: [10.1190/1.2742686](https://doi.org/10.1190/1.2742686).
- Symes, W. W., 2008, Approximate linearized inversion by optimal scaling of prestack depth migration: *Geophysics*, **73**, no. 2, R23–R35, doi: [10.1190/1.2836323](https://doi.org/10.1190/1.2836323).
- Symes, W. W., C. Stolk, B. Biondi, and F. Gao, 2003, Reverse time shot-geophone migration: *SEG-50*, 151–69.
- Tarantola, A., 1984, Inversion of seismic reflection data in the acoustic approximation: *Geophysics*, **49**, 1259–1266, doi: [10.1190/1.1441754](https://doi.org/10.1190/1.1441754).
- Ten-Kroode, A., D. Smith, and A. Verdel, 1998, A microlocal analysis of migration: *Wave Motion*, **28**, 149–172, doi: [10.1016/S0165-2125\(98\)00004-3](https://doi.org/10.1016/S0165-2125(98)00004-3).
- Wang, M., S. Huang, and P. Wang, 2017, Improved iterative least-squares migration using curvelet-domain Hessian filters: 87th Annual International Meeting, SEG, Expanded Abstracts, 4555–4560, doi: [10.1190/segam2017-17783350.1](https://doi.org/10.1190/segam2017-17783350.1).
- Wang, P., A. Gomes, Z. Zhang, and M. Wang, 2016, Least-squares RTM: Reality and possibilities for subsalt imaging: 86th Annual International Meeting, SEG, Expanded Abstracts, 4204–4209, doi: [10.1190/segam2016-13867926.1](https://doi.org/10.1190/segam2016-13867926.1).
- Whitmore, N., 1983, Iterative depth migration by backward time propagation: 53rd Annual International Meeting, SEG, Expanded Abstracts, 382–385, doi: [10.1190/1.1893867](https://doi.org/10.1190/1.1893867).
- Yang, J.-D., J.-P. Huang, X. Wang, and Z.-C. Li, 2015, An amplitude-preserved adaptive focused beam seismic migration method: *Petroleum Science*, **12**, 417–427, doi: [10.1007/s12182-015-0044-7](https://doi.org/10.1007/s12182-015-0044-7).
- Yoon, K., C. Shin, A. Suh, S. Lines, and S. Hong, 2003, 3-D reverse-time migration using the acoustic wave equation: An experience with the SEG/EAGE data set: *The Leading Edge*, **22**, 38–41, doi: [10.1190/1.1542754](https://doi.org/10.1190/1.1542754).
- Zhang, Y., S. Xu, N. Bleistein, and G. Zhang, 2007, True-amplitude, angle-domain, common-image gathers from one-way wave-equation migrations: *Geophysics*, **72**, no. 1, S49–S58, doi: [10.1190/1.2399371](https://doi.org/10.1190/1.2399371).



Hamideh Sanavi received an M.S. (2018) in geophysics from the Ferdowsi University of Mashhad, Mashhad, Iran. She has demonstrated excellence in researching, analyzing, and presenting information as a research assistant at the Ferdowsi University of Mashhad, focusing on the improvement of subsurface imaging technologies (focusing on prestack depth and prestack time migration techniques) since 2018.



Peyman P. Moghaddam received a B.S. (1995) and an M.S. (1998) from the Amirkabir University of Technology, Tehran, Iran, and a Ph.D. (2010) in geophysics from the University of British Columbia, Vancouver, Canada. After research positions at the University of British Columbia and Delft University of Technology in Delft, Netherlands, he worked for TGS in Houston, Texas, from 2013 till 2015. In 2015, he joined the Ferdowsi University of Mashhad, Faculty of Science, where he is now an assistant professor in geophysics. He is also a business development manager at BQI-FUM-Innovation Co. Ltd., a research-based company located in London, UK, which provides geoscience services. His research interests include seismic modeling, imaging and inversion, and high-performance computing methods for computationally intensive geoscientific applications.



Felix J. Herrmann graduated from the Delft University of Technology in 1992 and received a Ph.D. (1997) in engineering physics from that same institution. After research positions at Stanford University and the Massachusetts Institute of Technology, he became back in 2002 faculty at the University of British Columbia. In 2017, he joined the Georgia Institute of technology where he is now a Georgia Research Alliance Scholar Chair in Energy, cross-appointed between the Schools of Earth and Atmospheric Sciences, Computational Science and Engineering, and Electrical and Computer Engineering. His cross-disciplinary research program spans several areas of computational imaging including seismic, and more recently, medical imaging. Over his career, he has been responsible for several cost-saving innovations in industrial time-lapse seismic data acquisition and wave-equation based imaging. In 2019, he was the SEG Distinguished Lecturer and in 2020 the recipient of the SEG Reginald Fessenden Award. At Georgia Tech, he leads the Seismic Laboratory for imaging and modeling, and he is a cofounder/director of the Center for Machine Learning for Seismic (ML4Seismic).